Journal of Geophysical Research: Planets

Supporting Information for

Mineralogically Diverse and Salt-rich Regolith in Jezero Crater Characterized using X-ray Spectroscopy

Andrew O. Shumway*[1], Tanya V. Kizovski[2,3], David C. Catling[1], Scott J. VanBommel[4], Michael W. M. Jones[5], Brendan J. Orenstein[6,7], Mariek E. Schmidt[2], Michael M. Tice[8], Joel A. Hurowitz[9], Abigail L. Knight[4], Benton C. Clark[10], Lawrence Wade[11], Emily L. Cardarelli[12], An Y. Li[1], Mike J. Zawaski[8,13], David A. Klevang[14], William T. Elam[1,15], Elisabeth M. Hausrath[16], Allan H. Treiman[17], Jesper Henneke[14], Nicholas J. Tosca[18], Yang Liu[11], Morgan L. Cable[11], Abigail C. Allwood[11]

[1] Department of Earth & Space Sciences, University of Washington, Seattle, WA, USA
[2] Department of Earth Sciences, Brock University, St. Catharines, ON, Canada
[3] Department of Earth and Space, Royal Ontario Museum, Toronto, ON, Canada
[4] McDonnell Center for the Space Sciences, Department of Earth, Environmental, and Planetary Sciences, Washington University in St. Louis, St. Louis, MO, USA
[5] School of Chemistry and Physics and Central Analytical Research Facility, Queensland University of Technology, Brisbane, QLD, Australia
[6] School of Earth and Atmospheric Sciences, Queensland University of Technology, Brisbane, QLD, Australia
[7] Centre for Planetary Surface Exploration, Queensland University of Technology, Brisbane, QLD, Australia
[8] Department of Geology & Geophysics, Texas A&M University, College Station, TX, USA
[9] Department of Geosciences, Stony Brook University, Stony Brook, NY, USA
[10] Space Science Institute, Boulder, CO, USA
[11] Jet Propulsion Laboratory, California Institute of Technology, Pasadena, CA, USA
[12] Department of Earth, Planetary, and Space Sciences, University of California Los Angeles, Los Angeles, CA, USA
[13] Geosciences Department, Fort Lewis College, Durango, CO, USA
[14] Department of Space Research and Space Technology, DTU Space, Technical University of Denmark, Kongens Lyngby, Denmark
[15] Applied Physics Lab, University of Washington, Seattle, WA, USA
[16] Department of Geoscience, University of Nevada, Las Vegas, Las Vegas, NV, USA
[17] Lunar and Planetary Institute, Universities Space Research Association, Houston, TX, USA.
[18] Department of Earth Sciences, University of Cambridge, Cambridge, UK

Contents of this file

Text S1 to S4
Figures S1 to S4
Table S2

Additional Supporting Information (Files uploaded separately)

Table S1. Oxide abundances for individual PIXL measurements.

Table S3. Bulk sum oxide abundances for regions with similar composition.

Introduction

Included within are text, figures, and tables used to support the main text. All data, including separate file uploads for tables S1 and S3, are archived on NASA's Planetary Data System Geosciences node (https://pds-geosciences.wustl.edu/m2020/urn-nasa-pds-shumway_m2020_pixl_regolith/; https://doi.org/10.17189/esjs-6z59).

Text S1. Dust Layer Model

Identifying regolith mineralogy is complicated by the presence of dust, which affects PIXL's measurements of reflectance, diffraction, and composition. XRF measurements on a dusty surface result in a convolution of signals from the substrate and dust, which varies non-linearly with X-ray energy (e.g., atomic number; Berger et al., 2016; Knight et al., 2024; VanBommel et al., 2023). Instead, potential compositions of dust-free regolith were inferred through layering and deconvolution analyses on various likely substrates (VanBommel et al., 2022; 2023). Error bars are large and solutions are non-unique, but this method provides reasonable results when considered holistically alongside analysis of mixing trends, diffraction data, and reflectance results.

Text S2. K-means Clustering Algorithm

In order to delineate the various regolith components, individual PIXL measurements were sorted into categories based on similar composition and diffraction properties using a K-means clustering algorithm that was adapted from the Python package Scikit-Learn (Pedregosa et al., 2011). A K-means algorithm sorts data into "clusters" based on their proximity to iteratively-generated cluster centers in N-dimensional feature space. PIXL regolith data were clustered according to their elemental composition (wt. %) and whether or not diffraction peaks were identified at that point. For each element, compositional data were scaled to zero mean and a standard deviation of one, a typical data processing technique to ensure each feature (i.e., element or oxide) is evenly weighted in the clustering routine. This rescaling allows the algorithm to identify trends in minor elements (e.g., Cr) instead of being dominated by the most abundant elements. Diffraction data were binary (i.e., detected = 1, not detected = 0) and therefore did not need to be normalized.

The algorithm defined the clusters based on the *Marmot Bay* map dataset (sol 601), which was selected for its high density of measurements and diversity of compositions encountered (Fig. 5). The number of clusters was determined by repeatedly running the algorithm with two to nine clusters, then comparing the resulting clusters to MCC spectral data (Fig. 4) and RGB composition and diffraction maps (Fig. 5). The results best agreed with visible and compositional trends when the algorithm was set to identify six clusters. The first cluster is characterized by consistent diffraction peaks and a Fe, Mg-silicate composition. This cluster is populated by the ~1 mm, rounded, gray-ish grains in Fig. 4. The second cluster is notable for a lack of diffraction peaks, and a low-Fe, high-Si composition; the larger, angular, lighter-toned grains in Fig. 4 are sorted into this cluster. A third cluster groups points with no diffraction peaks and very high levels of Fe and Mg, with low levels of Si; two grains are sorted into this cluster. The fourth cluster identified a few small grains that are highly enriched in Cr and/or Ti. The fifth cluster groups most of the finer-grained material (grain size < 0.5 mm), which share a similar composition. The final cluster groups points with high levels of S, Cl, and P.

Next, we used the clustering routine based on the *Marmot Bay* map dataset to sort data from the remaining regolith scans into the six defined clusters. There are some limitations to this method, since every point will be sorted into the nearest cluster, even if the point represents a new composition not present in the original training dataset. When new grain types were present, we identified the outliers manually by inspecting their composition on binary and ternary diagrams. Overall, this method performed quite well at classifying regolith components across scans. For example, at *Topographers Peak*, which is mostly composed of finer-grained regolith, 96.7% of points (n = 1626) were classified in the same cluster as the fines at *Marmot Bay*. At *Ursus Cove*, the rounded gray grains that appear visibly and chemically similar to grains at *Marmot Bay* were reliably sorted into the same cluster.

Text S3. Chlorine Quantification

The quantification of Cl introduces an additional analytical burden in PIXL analyses due to spectral overlap between the Cl K_α line and backscattered Rh L lines (from the anode of PIXL's excitation source), which could lead to an overestimation of Cl. The contribution of backscattered X-rays from PIXL's Rh anode is considered during analysis and subsequent quantification by PIQUANT (Heirwegh et al., 2022), however small uncertainties in these line shapes can induce significant deviations in Cl attribution, especially at low wt. % Cl. PIQUANT's model of the fines spectrum produces a good match for the observed data, however, due to notable deviations from prior measurements, we do not rule out as-of-yet unknown potential errors that could result in PIXL over-quantifying Cl.

Text S4. Pyroxene

Across all three targets, PIXL measured a few points with compositions that follow a mixing trend towards an endmember that may be consistent with a pyroxene. However, due to small sample size (at most, three contiguous points with this composition) and compositional mixing with the surrounding fines, we cannot conclusively identify the mineral. Pyroxene could plausibly have been present, as it was detected in regolith across Jezero crater by the Mastcam-Z and SuperCam instruments (Cousin et al., 2025; Vaughan et al., 2023), and may have been present in the fines at *Observation Mountain* (Hausrath et al., 2025). SuperCam observations across the rover's traverse indicate that pyroxene was less common in regolith on the fan front than on the crater floor (Cousin et al., 2025), which could explain why PIXL data did not contain strong evidence of pyroxene.

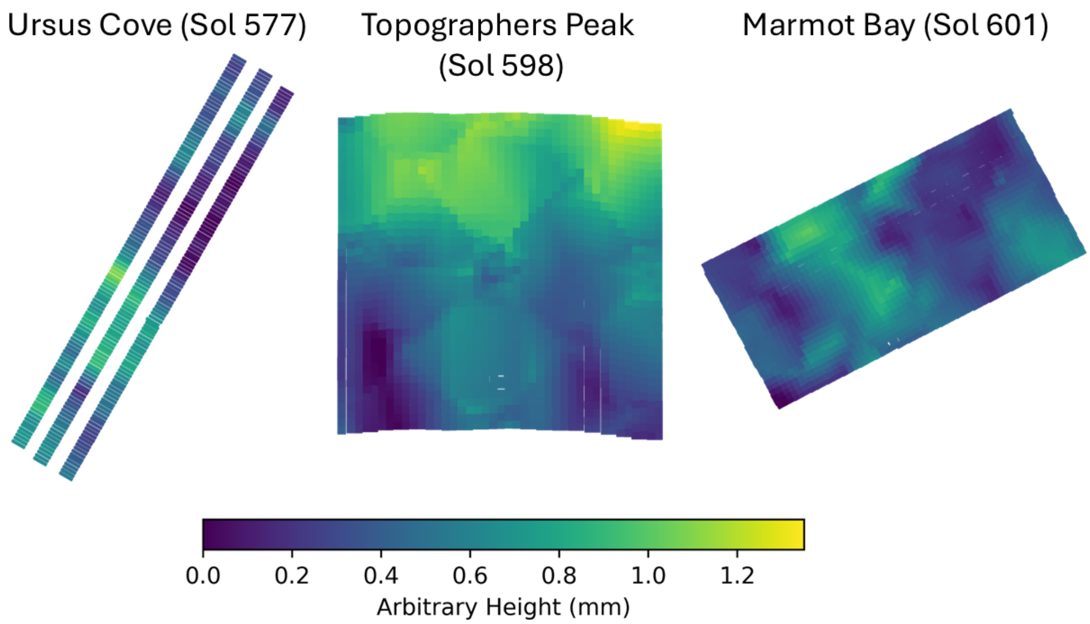

Figure S1. Topography maps of the regolith targets, based on the Z-location reported by PIXL. The lowest height value in each scan is rescaled to zero. The same color scale is applied across each scan.

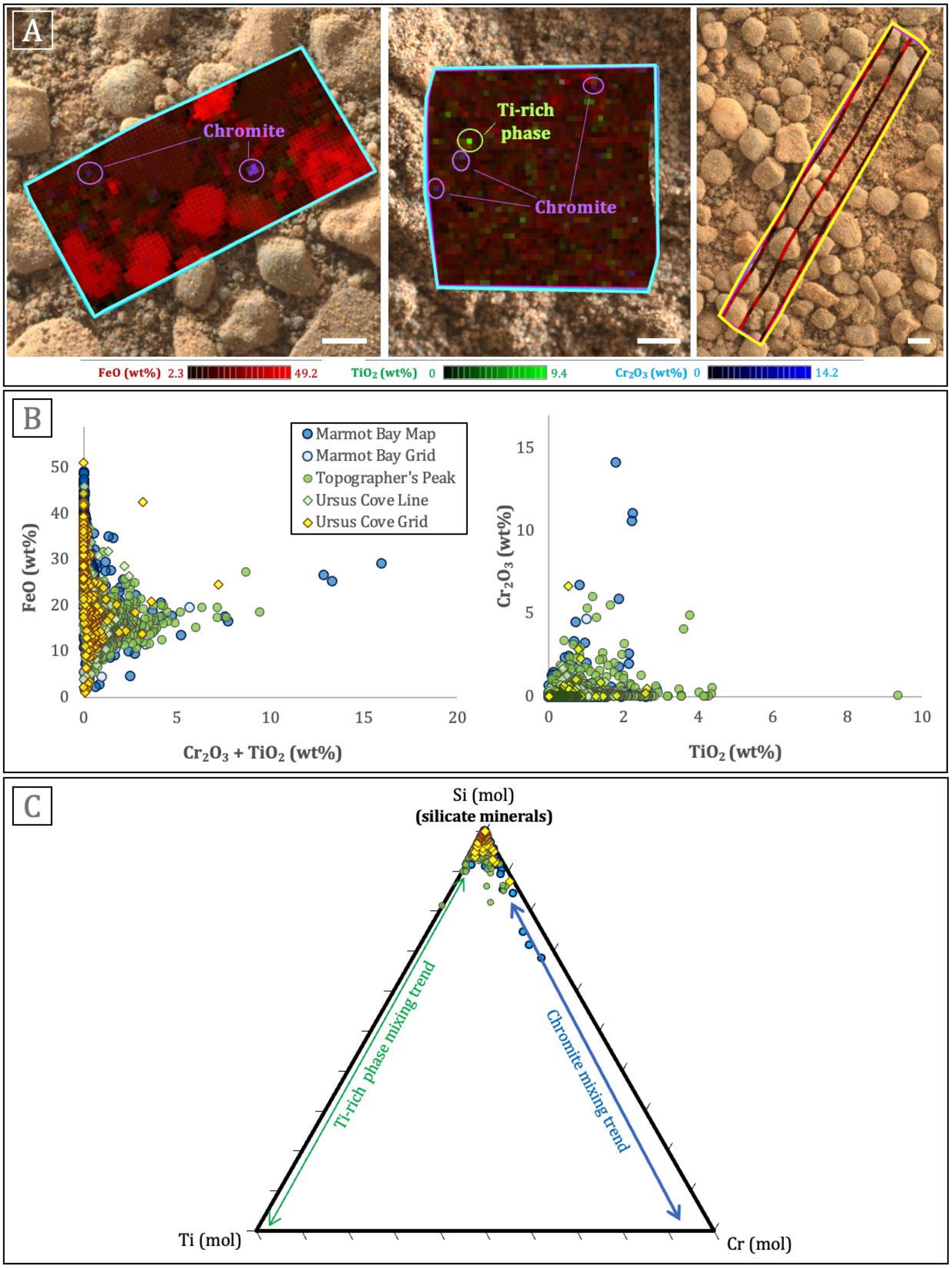

Figure S2. Chromite compositions. A) Color maps showing the abundance of FeO_T (red), TiO_2 (green), and Cr_2O_3 (blue), overlaid on WATSON images of the Marmot Bay, Topographers Peak, and Ursus Cove targets, respectively. White scale bar shows 1 mm. B) Plots of FeO_T vs. $Cr_2O_3 + TiO_2$ (wt. %) and Cr_2O_3 vs. TiO_2 (wt. %). Color and shape indicate which scan the data come from. C) Ternary plot of Si, Cr, and Ti (mol). Arrows show mixing trends towards pure chromite and an unidentified Ti-rich spinel phase. We identify spinels in seven points in *Marmot Bay*, four in *Topographers Peak*, and one in *Ursus Cove*.

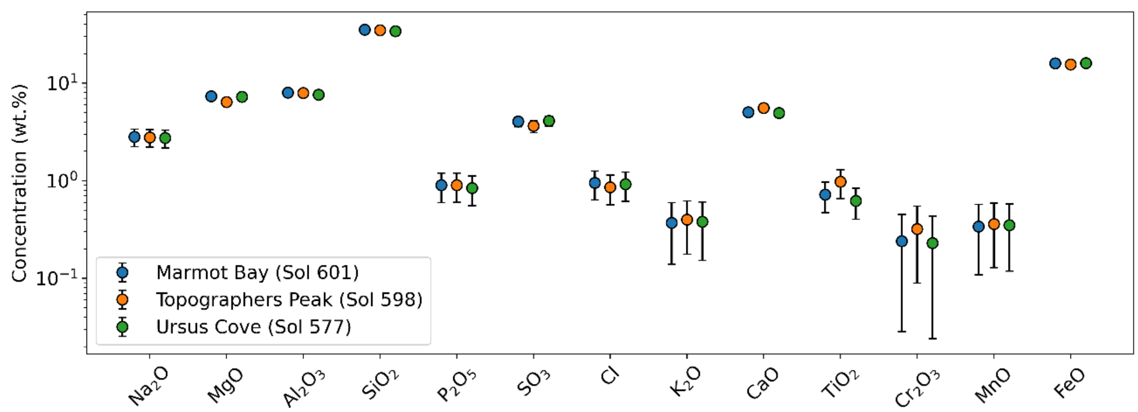

Figure S3. Comparison of finer-grained regolith fraction (i.e., soils) across three PIXL regolith targets. Soils at all three targets are geochemically uniform for all major elements, within uncertainties. Values and uncertainties are also reported in Table S3.

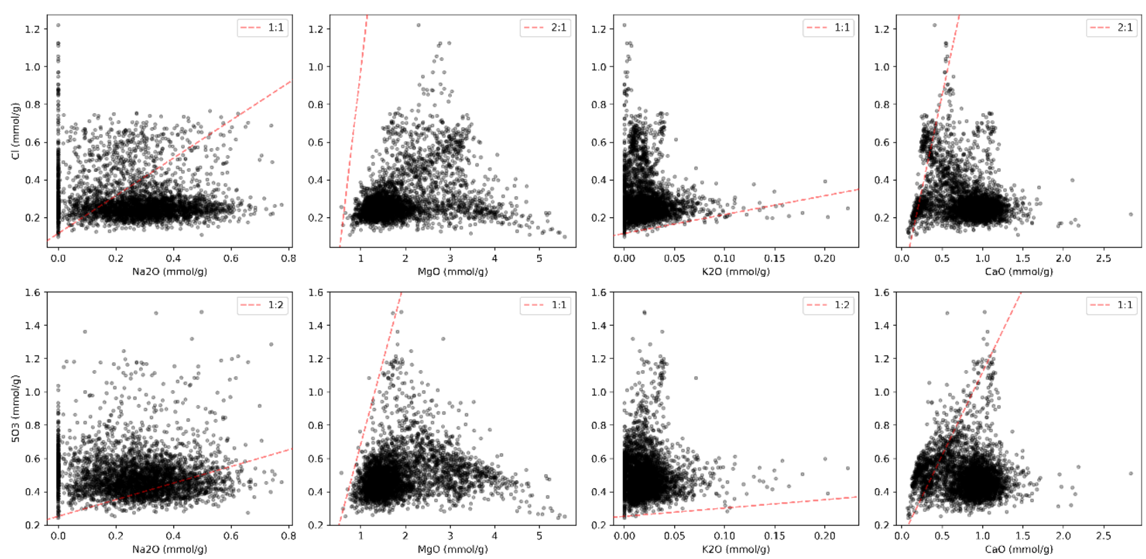

Figure S4. Scatter plots of all PIXL regolith measurements show correlations between various potential cations and SO_3 and Cl. Red dashed lines represent stoichiometric ratios of salts that would form from the two components (e.g., 1:2 for $CaCl_2$, or 1:1 for $MgSO_4$). Some high SO_3 points follow a 1:1 trend with Ca, suggesting calcium sulfates are plausible. This is consistent with previous interpretations of Ca-sulfate present in dust (Knight et al., 2024). Ca sulfate may also have been contributed from nearby *Yori Pass* style bedrock, which had veins of gypsum and anhydrite (Jones et al., 2025). Similarly, some high-Cl points follow a 2:1 molar trend with Ca, which is consistent with $CaCl_2$ and/or $Ca(ClO_4)_2$ (other oxychlorine phases are also possible). Both S and Cl correlate with K_2O at high K abundances, which is consistent with potassium chloride and/or perchlorate, as well as potassium sulfate. However, all K_2O abundances are < 0.25 mmol/g, so these would be minor phases. Neither S nor Cl correlate strongly with Na.

Table S1. (Separate upload: https://pds-geosciences.wustl.edu/m2020/urn-nasa-pds-shumway_m2020_pixl_regolith/data/; https://doi.org/10.17189/esjs-6z59) Oxide abundances for individual PIXL measurements across five regolith scans. Abundances have been corrected for effects caused by diffraction, topography, and roughness following the methodology described in Schmidt, et al. (2025). "PMC" stands for PIXL Motion Counter and is a unique integer assigned to each measurement within a scan. PMCs may be categorized into one of several regions of interest (ROIs) based on similar chemistry and diffraction properties (see section 3 of main text). ROIs were not assigned for the two grid scans (*Ursus Cove* sol 589 and Marmot *Bay* sol 600) because of low density of measurements and few spots on any single grain complicated identification of grain type. Uncertainties are reported from the PIQUANT software (Heirweigh et al., 2022).

Figure number	Target Name (Informal)	Instrument	Image ID
2A	*Ursus Cove*	Front Hazcam	FLF_0588_0719153024_565RAS_N0290000FHAZ00206_0A0295J01
2B	*Ursus Cove*	Mastcam-Z	ZLF_0566_0717178520_553RAS_N0290000ZCAM08587_0340LMJ01
2C	*Ursus Cove*	WATSON	SIF_0589_0719234796_609FDR_N0290000SRLC00451_0000LMJ01
3A	*Observation Mountain*	Front Hazcam	FLF_0599_0720116670_012RAS_N0300000FHAZ00206_0A0295J01
3B	*Observation Mountain*	Front Hazcam	FLF_0593_0719593428_996RAS_N0300000FHAZ02008_0A0095J01
3C	*Topographers Peak*	Mastcam-Z	SI1_0598_0720049360_660FDR_N0300000SRLC00071_000090J01
3D	*Topographers Peak*	WATSON	SI1_0598_0720049360_660FDR_N0300000SRLC00071_000090J01
3E	*Marmot Bay*	WATSON	SIF_0598_0720040845_183RAS_N0300000SRLC02504_0000LMJ01
3F	*Marmot Bay*	WATSON	SIF_0598_0720040987_687RAS_N0300000SRLC00604_0000LMJ01

Table S2. Image files used. Figure numbers correspond to figures in the main text.

Table S3. (Separate upload: https://pds-geosciences.wustl.edu/m2020/urn-nasa-pds-shumway_m2020_pixl_regolith/data/; https://doi.org/10.17189/esjs-6z59) Bulk sum oxide abundances for each region of interest (ROI).